

# The X-ray luminous cluster underlying the $z = 1.04$ quasar PKS 1229-021

H. R. Russell<sup>1\*</sup>, A. C. Fabian<sup>2</sup>, G. B. Taylor<sup>3</sup>, J. S. Sanders<sup>2</sup>, K. M. Blundell<sup>4</sup>, C. S. Crawford<sup>2</sup>, R. M. Johnstone<sup>2</sup> and E. Belsole<sup>2</sup>

<sup>1</sup> Department of Physics and Astronomy, University of Waterloo, Waterloo, ON N2L 3G1, Canada

<sup>2</sup> Institute of Astronomy, Madingley Road, Cambridge CB3 0HA

<sup>3</sup> Department of Physics and Astronomy, University of New Mexico, Albuquerque, NM 87131, USA

<sup>4</sup> University of Oxford, Department of Physics, Keble Road, Oxford OX1 3RH

27 October 2018

## ABSTRACT

We present a 100 ks *Chandra* observation studying the extended X-ray emission around the powerful  $z = 1.04$  quasar PKS 1229-021. The diffuse cluster X-ray emission can be traced out to  $\sim 15$  arcsec ( $\sim 120$  kpc) radius and there is a drop in the calculated hardness ratio inside the central 5 arcsec consistent with the presence of a cool core. Radio observations of the quasar show a strong core and a bright, one-sided jet leading to the SW hot spot and a second hot spot visible on the counter-jet side. Although the wings of the quasar PSF provided a significant contribution to the total X-ray flux at all radii where the extended cluster emission was detected, we were able to accurately subtract off the PSF emission using ChaRT and MARX simulations. The resulting steep cluster surface brightness profile for PKS 1229-021 appears similar to the profile for the FR II radio galaxy 3C 444, which has a similarly rapid surface brightness drop caused by a powerful shock surrounding the radio lobes (Croston et al.). Using a model surface brightness profile based on 3C 444, we estimated the total cluster luminosity for PKS 1229-021 to be  $L_X \sim 2 \times 10^{44}$  erg s<sup>-1</sup>. We discuss the difficulty of detecting cool core clusters, which host bright X-ray sources, in high redshift surveys.

**Key words:** X-rays: galaxies: clusters — galaxies: quasars: individual: PKS 1229-021 — intergalactic medium — cooling flows

## 1 INTRODUCTION

The bright quasar PKS 1229-021 (4C-02.55) at redshift  $z = 1.043$  is also a jetted radio source acting as a powerful gamma-ray source (Thompson et al. 1995; Celotti & Ghisellini 2008). On parsec-scales VLBA images show a strong compact core and a  $\sim 10$  mas jet to the west (Kovalev et al. 2007). Its extended radio structure was mapped at several frequencies with VLA by Kronberg et al. (1992). They attribute the observed variations in Faraday rotation measure across the source as due to an intervening absorber, having discounted the possibility that it is embedded in a cool core cluster on the grounds of the relaxed appearance for the radio source. A short (19 ks) archival *Chandra* image suggested the presence of extended X-ray emission (Tavecchio et al. 2007). Here we report on a 100 ks *Chandra* observation of the object clearly showing X-ray emission extended in a circular symmetric manner around the quasar. It is indeed hosted by a central cluster galaxy surrounded by hot intracluster gas. The hardness ratio of the X-ray emission drops towards the centre consistent with the cluster having a cool core.

Bauer et al (2005) found no evolution in the cooling time dis-

tribution at 50 kpc in cluster gas up to  $z \sim 0.4$ . Vikhlinin et al. (2007) searched for distant strong cool core clusters in the 400SD survey above  $z > 0.5$  and suggested that they are missing (see also Samuele et al. 2011). Recently, Santos et al. (2008) have measured the cool core fraction as a function of redshift using *Chandra* archival data out to  $0.7 < z < 1.4$  and find no drop in the total fraction, although they do not find any strong ones (i.e. Perseus-like clusters which have very strong cusps in X-ray surface brightness) at the higher redshifts (see also Alshino et al. 2010). These studies could indicate strong evolution in cool cores, perhaps requiring them to grow at lower redshift. An alternative explanation, which we address here, is that the strong cool core clusters at moderate to high redshift have active quasars at the centre. Due to the high brightness and superficial point-source appearance of such objects, the underlying cluster is then missing from cluster surveys, having been classified as quasars.

There is already evidence for clusters at the level of  $\sim 10^{44}$  erg s<sup>-1</sup> underlying several radio galaxies and radio-loud quasars at  $0.5 < z < 1$  (Crawford & Fabian 1996, 2003; Worral et al. 2003; Belsole et al. 2007; see also Wilkes et al. 2011). Siemiginowska et al. (2005) found a luminous,  $L_{0.5-2.0 \text{ keV}} \sim 6 \times 10^{44}$  erg s<sup>-1</sup>, cluster around the radio-loud quasar 3C 186 at

\* E-mail: helen.russell@uwaterloo.ca

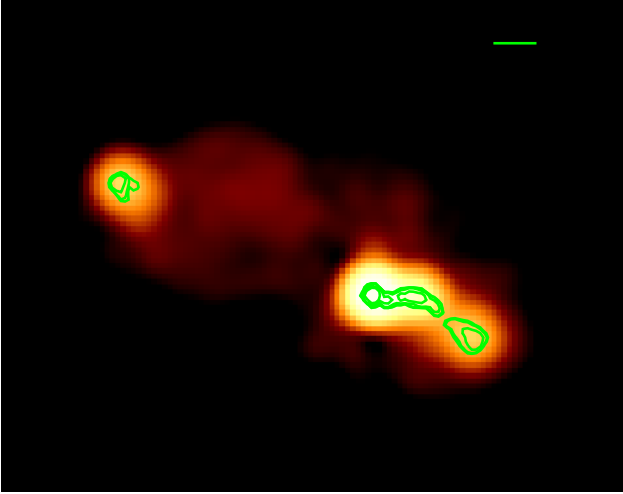


**Figure 1.** PKS 1229-021 at 1.4 GHz with emission at 8 GHz overlaid in green contours. North is up and East is to the left. The green line is 2.5 arcsec in length.

$z = 1.067$  and determined that it has a cool core with a central temperature drop from 8 to 3 keV (Siemiginowska et al. 2010). Here we report the results from a 100 ks *Chandra* observation of PKS 1229-021 which confirms the detection of extended emission around the luminous quasar. We discuss the radio observations in section 2, give details of the *Chandra* observations in section 3, describe the quasar PSF subtraction in section 4 and analyse the cluster emission in section 5. Finally, we consider the implications of these observations for surveys of galaxy clusters in section 6 and present our conclusions.

We assume  $H_0 = 70 \text{ km s}^{-1} \text{ Mpc}^{-1}$ ,  $\Omega_m = 0.3$  and  $\Omega_\Lambda = 0.7$ , translating to a scale of 8.09 kpc per arcsec at the redshift  $z = 1.043$  of PKS 1229-021. All errors are  $1\sigma$  unless otherwise noted.

## 2 THE RADIO SOURCE

PKS 1229-021 has a fairly typical morphology for a quasar with a strong core, and a bright, one-sided jet leading into a hot spot, and another hot spot visible on the counter-jet side (see 8 GHz map; Fig. 1). With its clear hotspots and a low frequency luminosity  $\sim 1$  dec above the FRI/II threshold (eg. Blundell & Rawlings 2001), PKS 1229-021 is a textbook example of an FRII radio source (Fanaroff & Riley 1974). The two most powerful FRII radio galaxies below  $z = 1$ , Cygnus A (Arnaud et al. 1984; Reynolds & Fabian 1996) and 3C 295 (eg. Henry & Henriksen 1986; Allen et al. 2001), are located in the centre of rich galaxy clusters. At higher redshifts, the environment of FRIIs could also be rich clusters and these powerful radio galaxies may act as markers of massive galaxy clusters (eg. Hall & Green 1998; Belsole et al. 2007). The jet in PKS 1229-021 is curved, suggesting perhaps a small intrinsic wiggle that has been exaggerated by a small angle to the line-of-sight, consistent with the quasar interpretation. This is supported by the pc-scale jet which shows a slight bend in the inner 10 mas but points in the general direction of the SW hot spot (eg. Fomalont et al. 2000). The arcsecond-scale core has a spectral index between 5 and 8 GHz of  $+0.31 \pm 0.05$ , while hot spots have values around -0.8 (Fig. 2). At 1.4 GHz some diffuse lobes are evident though the overall extent of the source is modest at an average of 20 arcsec ( $\sim 500$  kpc at  $z = 1.043$  for a reasonable angle to the line of sight; see Fig. 1).

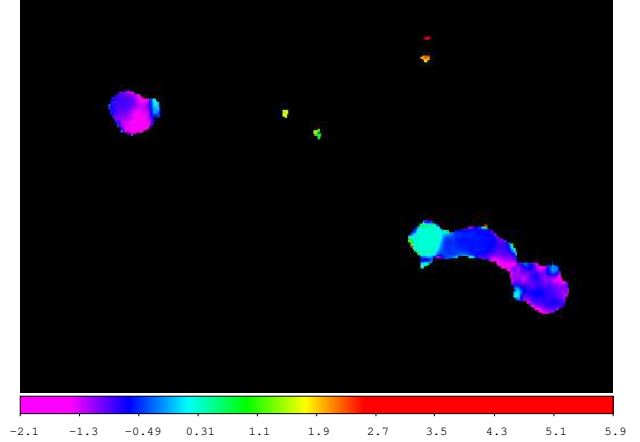


**Figure 2.** Spectral index map of PKS 1229-021.

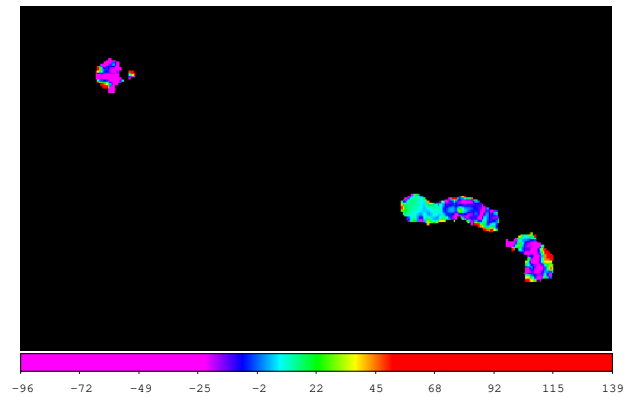


**Figure 3.** Rotation measure map of PKS 1229-021.

We have determined the Faraday Rotation Measure by combining polarimetry data from 4520, 4980, 8165, 8515 MHz at a common resolution of 0.45 arcsec. The source is well polarized at these frequencies (about 3 per cent in the core and 20 per cent in the hot spots). The eastern hot spot has an RM of  $-30 \text{ rad m}^{-2}$ , while the core has a value of  $11 \pm 1 \text{ rad m}^{-2}$  and the western jet has similar values between 0 and  $10 \text{ rad m}^{-2}$  (see Fig. 3). The western hot spot has an RM of  $-30 \text{ rad m}^{-2}$ . Even after multiplying by  $(1+z)^2$ , the intrinsic RMs are modest and range in absolute value from  $10 - 100 \text{ rad m}^{-2}$ . Our results are comparable to those of Kronberg et al. (1992) though ours are a bit more sensitive, thanks to additional data from the archive and improvements in processing techniques.

## 3 CHANDRA X-RAY OBSERVATIONS

PKS 1229-021 was observed by *Chandra* for a total of 100 ks split into two nearly equal length observations with ACIS-S taken eight days apart (Obs. IDs 11731 and 12205). The data were reduced using CIAO version 4.2 (Fruscione et al. 2006) and CALDB version 4.3.0 provided by the *Chandra* X-ray Center (CXC). The level 1 event files were reprocessed to apply the latest gain and charge transfer inefficiency correction and then filtered to remove photons detected with bad grades. The improved background screening provided by VFAINT mode was also applied. The background light

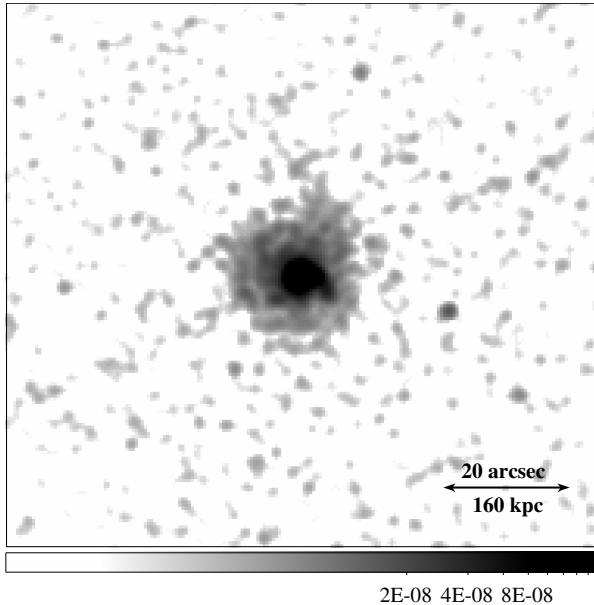


**Figure 4.** Exposure-corrected *Chandra* image of PKS 1229-021 in the energy range 0.5 – 7 keV smoothed by a 2D Gaussian with  $\sigma = 1.5$  arcsec (units  $\text{counts cm}^{-2} \text{s}^{-1} \text{pixel}^{-1}$ ). North is up and East is to the left. The faint line running from NW to SE through the centre of the source is the readout streak.

curve extracted from the ACIS-S1 level 2 event file was filtered using the `LC_CLEAN`<sup>1</sup> script produced by M. Markevitch to identify periods of the observation affected by flares. There were no flares found in either observation of PKS 1229-021 so we proceeded with the final cleaned exposure of 100 ks. The two separate observations were taken close together, with similar chip positions and roll angles, so we were able to reproject them to a common position (Obs. ID 11731) and combine them.

The radio-loud quasar PKS 1229-021 was detected as a bright X-ray point source in the combined image with a count rate high enough to generate pileup and a readout streak. Fig. 4 shows the combined *Chandra* X-ray image of PKS 1229-021. The X-ray emission peaks on the luminous quasar and there is a small spur of emission to the SW which clearly tracks the jet seen in the radio observations (see also Tavecchio et al. 2007). The extended emission, which is the focus of this work, is roughly circular and symmetric around the quasar point source and there is no obvious peak associated with the counter jet hotspot. The faint, straight line running across the image from NW to SE through the centre of the quasar is an instrumental artifact produced by the bright quasar. The count rate from the quasar is so high that a significant number of photons are arriving during the readout of each frame and producing a readout streak across the charge-coupled device (CCD).

The quasar’s high count rate also produces piled up events. Pileup occurs whenever two or more photons, arriving in the same detector region and within a single ACIS frame integration time, are detected as a single event (Davis 2001). Using a MARX simulation of the quasar that included a statistical treatment of pileup (section 4.2), we determined that pileup was only significant for the region inside 2 arcsec radius centred on the point source. To min-

imise the effects of pileup, this region was therefore excluded from our analysis.

#### 4 SUBTRACTING THE QUASAR PSF

The quasar point spread function (PSF) will likely dominate the X-ray emission inside 3 arcsec radius and provide a significant contribution to the source emission at all radii beyond this. It was therefore crucial to accurately understand and simulate the quasar PSF in order to analyse the underlying extended cluster emission. A detailed analysis of the *Chandra* PSF produced by the high resolution mirror assembly (HRMA) can be found on the CXC website<sup>2</sup>. In brief, the PSF can be approximately divided into two sections: a core produced by quasi-specular X-ray reflection from the mirror surface and wings generated by diffracted X-rays scattering from high frequency surface roughness. The PSF wings are therefore also energy dependent; the PSF is broader at high energies than at low energies.

We used the *Chandra* ray-tracing program ChaRT (Carter et al. 2003) to generate simulated observations with the HRMA and the MARX software<sup>3</sup> version 4.5 to project the ray-tracings onto the ACIS-S detector. This allowed us to analyse the spatial and energy dependence of the PSF in the absence of the extended cluster emission. ChaRT takes as inputs the position of the point source on the chip, the exposure time and the spectrum of the quasar.

##### 4.1 Quasar spectrum

As the core of the PKS 1229-021 observation is piled up, the quasar spectrum could not be determined simply from a small, quasar-dominated region on the chip. Instead, we determined the unpiled up quasar flux from the readout streak (suggested by M. Bautz, see Marshall et al. 2005; Gaetz 2010) as previously shown for the observation of the quasar H1821+643 in Russell et al. (2010). For this observation of PKS 1229-021, ACIS accumulated events for a frame exposure time of 3.1 s and then read out the frame at a parallel transfer rate of 40  $\mu\text{s}$ , taking a total of 0.04104 s to read out the complete frame. During readout, the CCD is still accumulating events which are distributed along the whole column as it is read out. This creates a continuous streak for very bright point sources. However, the X-ray flux from the point source PKS 1229-021 was at least an order of magnitude lower than H1821+643, therefore there were only sufficient counts in the readout streak to estimate the flux rather than produce a complete spectrum.

The readout streak count rate in the energy range 0.5 – 7.0 keV was extracted from three narrow regions,  $400 \times 8 \text{ pixel}^2$  NW of the quasar and two  $200 \times 8 \text{ pixel}^2$  regions to the SE, avoiding a low count rate background point source and the region of extended cluster emission. The background point source was not bright enough to contribute a significant number of counts to the readout streak. The background emission in the readout streak was subtracted using background regions positioned adjacent to the streak. The accumulated exposure time in the readout streak during frame transfer was  $(3.1 \text{ s} \times 100 \text{ ks}) / ((400 + 200 + 200) \times 40 \mu\text{s}) = 1027.3 \text{ s}$ , where the total exposure time for the observation was 100 ks. The readout streak flux was corrected for the mean exposure at the position of the quasar image. The X-rays in the readout streak hit the detector

<sup>1</sup> See <http://cxc.harvard.edu/contrib/maxim/acisbg>

<sup>2</sup> See <http://cxc.harvard.edu/cal/Hrma/UsersGuide.html>

<sup>3</sup> See <http://space.mit.edu/CXC/MARX>

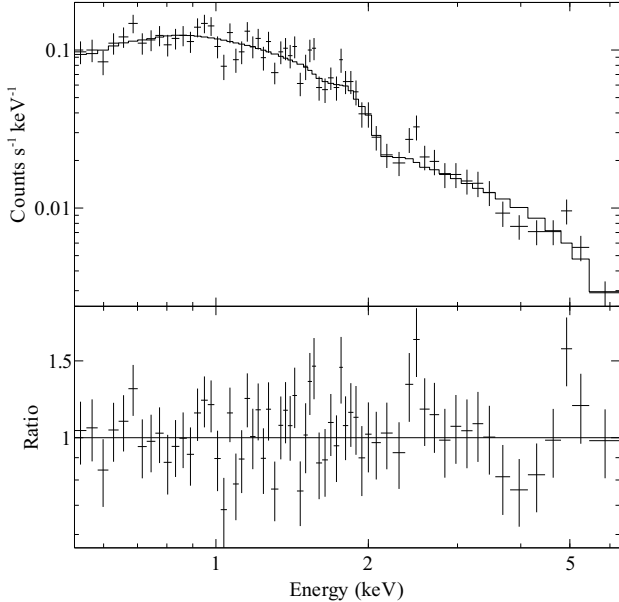


**Figure 5.** PKS 1229-021 spectrum extracted from obs. ID 4841 with the best-fit power-law model.

at the direct image and their detected position is an artifact of the chip readout.

The earlier *Chandra* observation of PKS 1229-021 analysed by Tavecchio et al. (2007) and available in the *Chandra* archive (Obs. ID 4841, 19 ks, taken in April 2004), is not affected by pileup. The analysis was focussed on the point source rather than the extended emission and therefore the chip was windowed and the frame time of the observation was reduced to 0.4 s. This archival observation was reduced following the method outlined in section 3 to apply the latest calibrations. A spectrum of the quasar was extracted from a region of 1.5 arcsec radius, which contains over 90 per cent of the PSF flux and is dominated by the point source emission. The spectrum was analysed in the energy range 0.5 – 7.0 keV, grouped with a minimum of 30 counts per spectral bin and background subtracted using neighbouring regions. Response and ancillary response files were generated, weighted according to the number of counts between 0.5 and 7.0 keV.

The resulting spectrum was fitted with an absorbed power-law model in XSPEC version 12.5.0 (Arnaud 1996). The best-fit model, with reduced  $\chi^2 = 1.1$ , was consistent with the results from Tavecchio et al. (2007) with a photon index  $\Gamma = 1.60 \pm 0.06$ ,  $n_{\text{H}} = 0.01^{+0.02}_{-0.01} \times 10^{22} \text{ cm}^{-2}$  and unabsorbed energy flux  $F_{2-10 \text{ keV}} = 1.07 \pm 0.06 \times 10^{-12} \text{ erg cm}^{-2} \text{ s}^{-1}$  (Fig. 5). Assuming that the absorption and photon index for the quasar have not varied since the *Chandra* observation in 2004, we used a power-law model with these parameters and set the model flux in the 0.5 – 7.0 keV energy band to match the readout streak flux from the new *Chandra* observations. This produced an unabsorbed energy flux determined from the readout streak of  $F_{2-10 \text{ keV}} = 1.1 \pm 0.1 \times 10^{-12} \text{ erg cm}^{-2} \text{ s}^{-1}$ , which is consistent with the observation in 2004 and suggests there hasn't been a significant variation in the quasar flux. We therefore used the spectral model from the 2004 observation as the input to the ChaRT simulation of the quasar.

## 4.2 ChaRT simulations

The *Chandra* Ray Tracer (ChaRT) was used to simulate the *Chandra* PSF produced by the quasar. Following the ChaRT analysis threads<sup>4</sup>, we used the source position on the chip and the model spectrum from Tavecchio et al. (2007), which is consistent with the readout streak count rate, to generate a ray-tracing simulation. The simulation was run for an exposure time of 200 ks to reduce statistical errors. The output from ChaRT was then supplied to MARX version 4.5 which projects the ray traces onto the detector to produce an events file and applies the detector response.

ChaRT uses the SAOTrace semi-empirical model (Jerius et al. 1995), which is based on the measured characteristics of the mirrors, support structures and baffles. This model is then calibrated by comparison with observations. The PSF core and inner wing region match well with observations (Jerius 2002) and should be well modelled. However, the model appears to underpredict the flux in the wings at energies above 3 keV and for large off-axis angles (Gaetz 2010). For our analysis of PKS 1229-021, we produce radial profiles out to only  $\sim 20$  arcsec (section 5.1) and observe photon energies predominantly less than 3 keV so the raytrace simulation should be sufficiently accurate.

The SAOTrace model does not currently account for the dither motion of the telescope or include residual blur from aspect reconstruction errors. These effects are approximated by the MARX DitherBlur parameter, which is a statistical term combining the aspect reconstruction error, ACIS pixelization and pipeline pixel randomization. Although the magnitude of the aspect blur is observation dependent, the DitherBlur parameter was left at its default value of 0.35 arcsec as reasonable variations of  $\pm 0.1$  arcsec were all found to be consistent within the statistical errors.

We also confirmed our earlier analysis in section 3 that pileup was not important beyond a radius of 2 arcsec from the quasar by generating a MARX simulation of the source which included pileup.

## 5 CLUSTER EMISSION ANALYSIS

The ChaRT simulations were used to subtract the contribution of the bright quasar PSF and enable a study of the underlying extended cluster emission. It is plausible that some of the extended emission in PKS 1229-021 is due to inverse Compton scattering on Cosmic Microwave photons (ICM), which is difficult to separate from X-ray cluster gas. We discuss this issue in detail in section 5.4 and conclude that, although some of the extended emission could be due to ICM, the hardness ratio analysis suggests that ICM is unlikely to dominate over thermal emission. However, the flux measurements in section 5.1 could contain a component of ICM emission and should be treated as upper limits.

### 5.1 Surface brightness profile

The total surface brightness profile was extracted from the exposure-corrected image for PKS 1229-021 using a sector centred on the quasar and excluding the SW X-ray jet emission (Fig. 6). The radial bins are 1 arcsec wide in the centre and increase in size at large radii where the background becomes more important. The CIAO algorithm WAVDETECT was used to identify point sources in the image (Freeman et al. 2002); no point sources, apart from the

<sup>4</sup> See <http://cxc.harvard.edu/chart/>

quasar source, were found in the region analysed around PKS 1229-021. The background was subtracted using the count rate extracted in a sector at larger radii free of source emission, 220 – 295 arcsec. The surface brightness profile for the quasar PSF was extracted from the ChaRT simulation using the same sector and regions.

The excess emission from the cluster can be seen over the quasar PSF from  $\sim 3 - 14$  arcsec radius (Fig. 6). The total flux in the sector from  $\sim 3 - 14$  arcsec radius is  $F_T = 2.5 \pm 0.1 \times 10^{-8}$  counts  $\text{cm}^{-2} \text{s}^{-1} \text{arcsec}^{-2}$  and the PSF flux in this region is  $F_{\text{PSF}} = 1.30 \pm 0.04 \times 10^{-8}$  counts  $\text{cm}^{-2} \text{s}^{-1} \text{arcsec}^{-2}$ . Subtracting the PSF contribution, the cluster emission from  $3 - 14$  arcsec radius in this sector is  $F_C = 1.20 \pm 0.06 \times 10^{-8}$  counts  $\text{cm}^{-2} \text{s}^{-1} \text{arcsec}^{-2}$ . The cluster emission is therefore comparable to the PSF flux in this region.

To calculate the total luminosity for the underlying cluster, we need a model for the surface brightness profile which extrapolates over the radii affected by pileup and can be fitted to the observed profile. However, the steep decline in the underlying cluster surface brightness from  $10 - 20$  arcsec was difficult to match with a typical cluster profile, even for a strong cool core cluster such as RXCJ 1504.1-0248 (Böhringer et al. 2005). We instead produced a model based on the surface brightness profile of the powerful radio galaxy 3C444, which contains a large-scale shock surrounding the radio lobes (Croston et al. 2011). Fig. 7 shows the surface brightness profile for 3C444 extracted using complete annuli centred on the X-ray peak from *Chandra* obs. id 11506, which was reduced using a method similar to Croston et al. (2011) (see section 3). We fitted this surface brightness profile with a  $\beta$ -model (Cavaliere & Fusco-Femiano 1976), where  $\beta = 0.7$ , plus a Gaussian component at 90 kpc, which accounts for the steepening of the profile at the shock front. Ideally, for a shock front with a radius that varies as a function of position angle, the surface brightness profile would be analysed in sectors (as in Croston et al. 2011). However, beyond 2 arcsec radius, for PKS 1229-021 there are a total of  $\sim 1600$  counts in the energy range  $0.5 - 7$  keV of which only  $\sim 750$  counts are from the extended emission (compare with  $\sim 7000$  counts for 3C444). It was therefore not feasible to analyse the surface brightness profile of PKS 1229-021 in sectors and we therefore used the Gaussian component to model the azimuthal average of the shock edge about a mean radius. The central 20 kpc region of 3C444 was excluded from this model fit as this region strongly deviates from the model and corresponds to the region affected by pileup in PKS 1229-021. It was therefore not possible to determine if the central region of PKS 1229-021 also has a rapidly steepening surface brightness profile. The model surface brightness profile for PKS 1229-021 shown in Fig. 8 is therefore conservative and could be underestimating the total cluster flux in the centre.

For PKS 1229-021, we added the cluster model ( $\beta$ -model plus Gaussian component) to the PSF simulation and fitted the combined model profile to the observed surface brightness profile. The  $\beta$ -model characteristic radius, width of the Gaussian component and the normalization of both components were left free. The value of  $\beta$  was fixed to 0.7 and the radius of the Gaussian component was fixed to 50 kpc. Fig. 8 shows the resulting best-fit model, with  $\chi^2 = 19$  for 21 degrees of freedom, compared to the observed total surface brightness profile. The radius of the best-fit Gaussian component approximately coincides with the edge of the 1.4 GHz radio emission from the SW jet. However, this putative shock edge is broad with a width of  $\sim 25$  kpc, which is likely due to the variation in the shock radius with position angle but is also consistent with the quasar interpretation where the shock is observed perpendicular to the line of sight. Fig. 8 shows that the Gaussian component

produces a surface brightness jump by a factor of  $\sim 1.5$ , which corresponds to a density jump of  $\sim 1.3$ . Using the density jump and the Rankine-Hugoniot shock jump conditions (eg. Landau & Lifshitz 1959; Markevitch & Vikhlinin 2007), we estimate that this produces a temperature jump by a factor of  $\sim 1.2$ . This is likely to be very difficult to measure given the low number of counts from the cluster emission and the smearing of the shock edge caused by the variation in radius.

By integrating this cluster surface brightness model for PKS 1229-021 out to 1 Mpc radius, which covers the vast majority of the emission, the absorbed cluster X-ray photon flux is estimated to be  $F_{0.5-7\text{keV}} \sim 9 \times 10^{-6}$  photons  $\text{cm}^{-2} \text{s}^{-1}$ .

## 5.2 Spectral analysis

We extracted a global spectrum of the cluster using a region from  $3 - 8$  arcsec radius, which excluded the SW jet and the centre affected by pileup. The background was subtracted using a spectrum extracted from a cluster-free region at the edge of the chip as in section 5.1. Appropriate responses and ancillary responses were generated with CIAO and the spectrum was restricted to the energy range  $0.5 - 7.0$  keV. The spectrum was fitted in XSPEC with an absorbed power-law model, to account for the quasar PSF, and an absorbed thermal plasma emission model for the cluster PHABS(POWERLAW) + PHABS(MEKAL) (Balucinska-Church & McCammon 1992; Mewe et al. 1985, 1986; Kaastra 1992; Liedahl et al. 1995). Abundances were measured assuming the abundance ratios of Anders & Grevesse (1989), the redshift was fixed to  $z = 1.043$  and the absorption column density component for the cluster emission was fixed to the Galactic value  $n_{\text{H}} = 0.02 \times 10^{22} \text{cm}^{-2}$  (Kalberla et al. 2005).

Allowing the parameters describing the quasar PSF to freely vary produced a power-law normalization that was a factor of two greater than expected for the PSF. This suggests that the cluster emission has been incorrectly interpreted as PSF emission in the spectral fitting. Therefore, we used the ChaRT simulations to produce a spectrum of the PSF in this region and fitted this with an absorbed powerlaw model to determine the appropriate parameters (eg. Russell et al. 2010). ChaRT was run for an effective exposure time six times longer than the total exposure time to sample the range of possible optical paths in the HRMA and reduce statistical errors. Suitable response files were generated for the simulated spectrum with MARX and the energy range was restricted to  $0.5 - 7.0$  keV. The low number of counts in each loaded spectrum required the use of the C-statistic (Cash 1979). The best-fit model produced a photon index  $\Gamma = 1.26_{-0.07}^{+0.06}$ , absorption  $n_{\text{H}} = 0.02 \pm 0.02 \times 10^{22} \text{cm}^{-2}$  and normalization  $3.3 \pm 0.2 \times 10^{-6}$  photons  $\text{keV}^{-1} \text{cm}^{-2} \text{s}^{-1}$  at 1 keV. These best-fit parameters for the analysed region differ from the ChaRT input PSF spectrum for the quasar because the effective area calculation assumes that all of the PSF falls within the extraction region. Here we are considering only the PSF wings from  $3 - 8$  arcsec radius.

The parameters describing the absorbed power-law component of the combined PSF and cluster emission model were fixed to these best-fit values determined from the PSF simulation. The temperature, metallicity and normalization of the MEKAL model component were left free and the C-statistic was used to determine the best-fit. The best-fit model gave a cluster temperature of  $6_{-2}^{+3}$  keV and an upper limit on the metallicity of  $0.6Z_{\odot}$ . We calculated the total luminosity of the cluster using an absorbed MEKAL model with temperature of 6 keV and metallicity  $0.3Z_{\odot}$ . The normaliza-

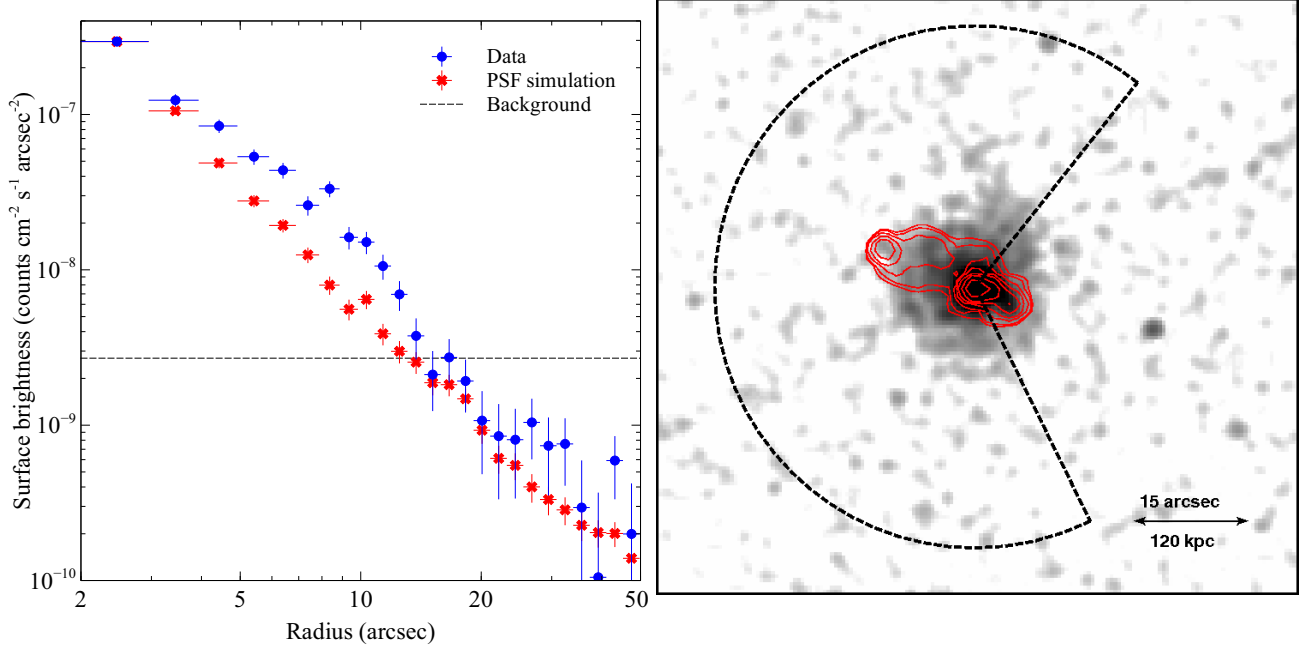


**Figure 6.** Left: Background-subtracted surface brightness profile in the energy range 0.5 – 7.0 keV for PKS 1229-021. Radii inside 2 arcsec are affected by pileup. Right: Exposure-corrected image of PKS 1229-021 overlaid with VLA 1.4 GHz radio contours (narrow lines) and the sector used to extract the surface brightness profile extending over 50 – 295 deg (thick dashed lines). The faint line extending across the image from SE to NW through the centre of the source is the readout streak.

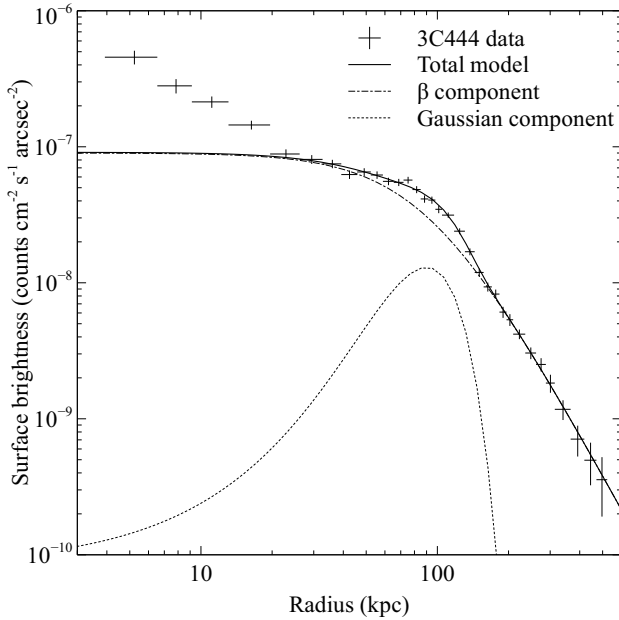


**Figure 7.** Surface brightness profile for 3C444 in the energy band 0.5 – 7.0 keV. The best-fit  $\beta$ -model with an additional Gaussian component for shock is shown as the solid line.

tion was set so that the model’s absorbed flux corresponded to that determined in section 5.1. The total cluster luminosity was therefore calculated to be  $L_X \sim 2 \times 10^{44} \text{ erg s}^{-1}$  for the energy range 0.05 – 50 keV. The  $L_X - T$  relation typically observed in high-redshift clusters predicts a temperature of 2 – 3 keV for a cluster with this luminosity, which appears lower than expected from the measured temperature of  $6_{-2}^{+3}$  keV (eg. Vikhlinin et al. 2002; Lumb

et al. 2004). Fig. 8 suggests that the radial region in which the temperature has been measured corresponds to the position of the shock. For 3C 444, the global temperature of the extended emission is  $3.5 \pm 0.2$  keV but the temperature in the shock region is significantly higher at 5 – 6 keV (Croston et al. 2010). By measuring the temperature for PKS 1229-021 in a region dominated by the shock we will likely be biasing the measurement high.

The unabsorbed energy flux of the cluster in the sector from 3 – 8 arcsec radius is  $F_{0.01-50 \text{ keV}} = 1.7_{-0.2}^{+0.5} \times 10^{-14} \text{ erg cm}^{-2} \text{ s}^{-1}$ . Assuming a spherical galaxy cluster and correcting for a complete spherical shell, the electron density is then  $n_e = 0.016_{-0.001}^{+0.002} \text{ cm}^{-3}$ . This gives a radiative gas cooling time of  $6_{-2}^{+4}$  Gyr and a classical mass deposition rate of  $\dot{M}_I = 90_{-30}^{+50} M_\odot$  from 24 – 65 kpc radius.

We evaluated the impact of uncertainty in the quasar PSF subtraction on these results by repeating the model fit with a  $\pm 10\%$  variation in the normalization of the power-law component. A  $\pm 10\%$  variation samples the uncertainty in the analysis of the quasar spectrum (section 4.1) which produces corresponding uncertainty in the PSF spectrum extracted for the sector from 3 – 8 arcsec radius. This variation produced an additional uncertainty in the temperature estimate of  $\pm 2$  keV, comparable to the statistical error, and similarly an uncertainty in the energy flux,  $F_{0.01-50 \text{ keV}}$ , of  $\pm 0.4 \times 10^{-14} \text{ erg cm}^{-2} \text{ s}^{-1}$ . The quasar PSF provides a significant contribution to the flux at all radii where cluster emission is detected and an accurate subtraction is therefore critical for determining the cluster properties.

The outer radius of 8 arcsec was selected as a conservative limit to exclude the region of the PSF wings that are underestimated by the ChaRT simulations at high energies (section 4.2). If the outer radius of the region is increased from 8 arcsec to 14 arcsec the best-fit cluster temperature rises to  $10_{-3}^{+9}$  keV. This could be due to a real increase in the gas temperature however it seems implausibly high compared to the prediction from the  $L_X - T$  relation. Alternatively,

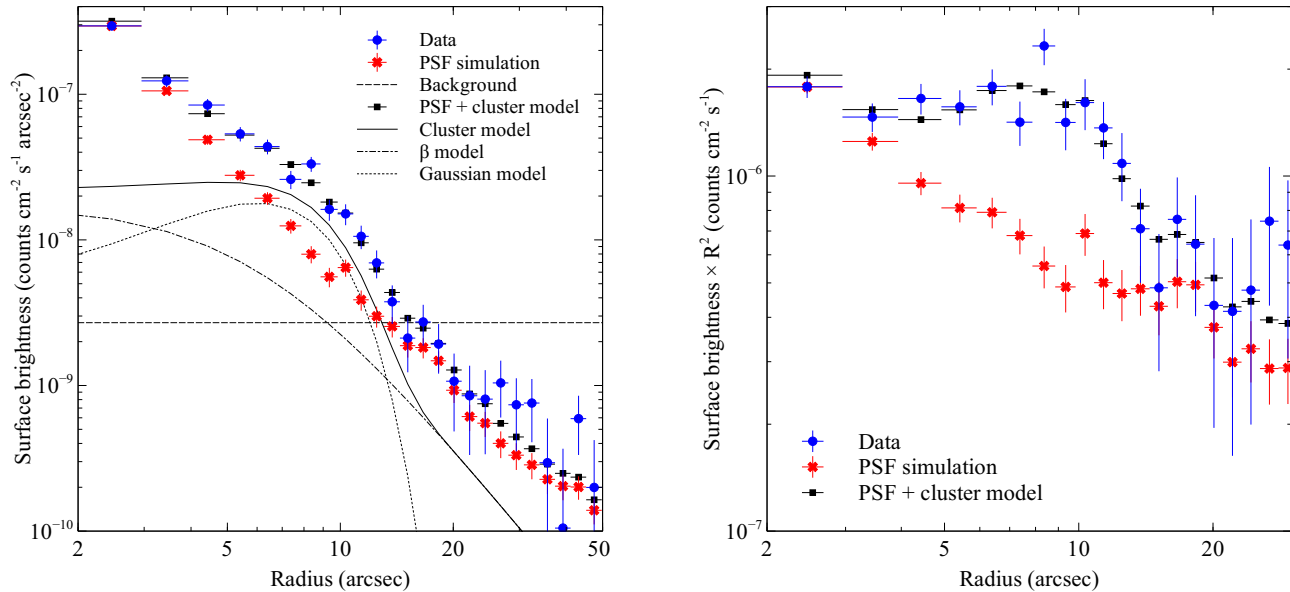


**Figure 8.** Left: Surface brightness profile for PKS 1229-021 in the energy band 0.5 – 7.0 keV. The best-fit model for the extended cluster emission (solid line) and this model added to the PSF simulation (squares) are shown overlaid. Right: Surface brightness profile multiplied by the square of the bin radius showing the agreement between the PKS 1229-021 observation and the PSF simulation plus the cluster model.

this could be the result of an undersubtraction of the PSF in the 5 – 7 keV energy band leaving extra high energy counts to be fitted with the cluster spectral model. Repeating the spectral fit with the energy range restricted to 0.5 – 5 keV reduces the temperature to  $7_{-2}^{+4}$  keV.

Unfortunately, the low number of cluster counts prevented us from subdividing this spatial region and extracting spectra from multiple radial bins to determine if the underlying cluster has a significant temperature gradient. We therefore calculated the hardness ratio profile to determine if there were any variations indicative of a temperature gradient.

### 5.3 Hardness ratio profiles

The hardness ratio, comparing numbers of counts observed in different energy bands, is useful to characterize weak sources for which detailed spectral fitting is not feasible. We used the Bayesian method of calculating hardness ratios described in Park et al. (2006), which treats the detected counts as independent Poisson random variables and correctly propagates errors for the low counts regime. The hardness ratio was calculated using the fractional difference between the counts in the soft ( $S$ ) and hard ( $H$ ) energy bands,

$$HR \equiv \frac{H - S}{H + S}. \quad (1)$$

The source count rates in each energy band were extracted from radial bins of 1 arcsec width in the sector which excluded the SW X-ray jet emission (Fig. 6). The radial bins increase in size at large radii where the background becomes more important. A second set of wider radial bins were also used as a test of the robustness and significance of the result. The hardness ratio was calculated using a soft energy band, 0.5 – 1.5 keV, and a hard energy band, 1.5 – 5.0 keV. These passbands were selected to produce a similar number of counts in each radial bin on average across the ra-

dial profile. The observed background counts, including the quasar PSF contribution, were also modelled as independent Poisson random variables. The background count rate was determined from a large source-free region as described in section 5.1. The quasar PSF count rates were extracted from the ChaRT simulations using the same radial regions as for the source count rates. A correction factor was included to account for the relative size of the source and background regions and for the longer exposure time of the simulated PSF.

Fig. 9 shows a significant drop in the hardness ratio inside the central 5 arcsec radius of PKS 1229-021. The decline in hardness ratio corresponds to an increase in the fraction of low energy photons in the cluster centre and a drop in the gas temperature, roughly from  $\sim 8$  keV to  $\sim 2$  keV. If a shock driven by the central source has expanded through the cluster gas then we would expect the core ICM to be heated, unless this material was originally cool. We therefore suggest that this steep decline in the hardness ratio inside 5 arcsec radius is consistent with the presence of a cool core. The estimated  $\pm 10\%$  error in the quasar PSF flux does not have a significant effect on the hardness ratio profile out to 20 arcsec and the central decline in the hardness ratio is robust to the estimated errors in the PSF simulation.

### 5.4 Inverse-Compton emission

Extended radio sources at high redshift are often detected in the X-ray band due to inverse Compton scattering on Cosmic Microwave Background photons (ICMB process; see e.g. Croston et al. 2005; Erlund et al. 2008). It is possible that some of the extended X-ray emission reported here has a similar origin. The SW X-ray spur extending from the point source lines up clearly with the SW radio jet suggesting an inverse Compton origin for this emission, therefore this region was excluded from our analysis of the cluster emission (Fig. 6). We note, however, that the surrounding X-ray emission is much more symmetrical than the radio source and the drop in hardness ratio within 5 arcsec, where ICMB could be most important

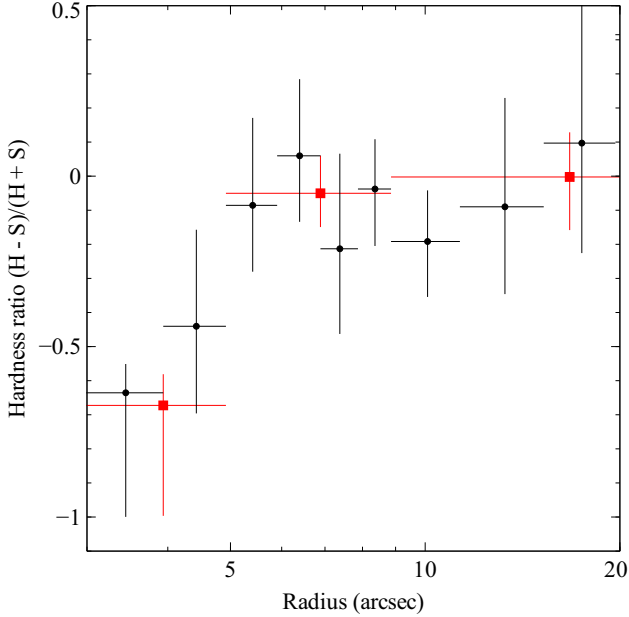


**Figure 9.** Hardness ratio profile using soft energy band 0.5 – 1.5 keV ( $S$ ) and hard energy band 1.5 – 5.0 keV ( $H$ ) for 1 arcsec (circles) and 2 arcsec wide radial bins (squares).

requires a steep spectral index to the electron population. A photon index  $\Gamma = 1.7$  corresponding to a radio synchrotron or X-ray IC-CMB spectral index of 0.7, has a hardness ratio of -0.19, which is harder than observed. To become steeper than -0.5 requires  $\Gamma$  to exceed 2.5. Also, the hardness ratio for the excluded SW X-ray spur, which lines up with the SW radio jet, is approximately -0.25. The central softening we see is not then simply due to ICCMB emission (or indeed scattered photons from the nucleus which has  $\Gamma = 1.6$  corresponding to a hardness ratio of -0.15).

At larger radii, where the radio emission drops off, there could be an older electron population producing IC emission. However, the hardness ratio observed outside  $5''$  radius appears too soft,  $-0.05 - 0$  (Fig. 9), compared to the hardness ratio found in the jet. The diffuse X-ray emission around the powerful FR II radio source 3C 294 at  $z = 1.786$ , for example, has a thermal temperature of 3.5 keV, much lower than the  $\sim 6 - 8$  keV seen at large radii in PKS 1229-021, and could feasibly be instead due to IC emission with  $\Gamma = 2.3$  (Fabian et al. 2003).

We therefore conclude that some of the extended emission in PKS 1229-021 could feasibly be due to ICCMB rather than cluster gas. The flux measurements in section 5.1 are therefore upper limits on the thermal emission and could contain a component of ICCMB. However, the calculated hardness ratio is too soft inside the central 5 arcsec, where ICCMB could be most important, and too hard at larger radii to be produced primarily by ICCMB.

### 5.5 Magnetic field estimate

Using the Faraday Rotation Measure determined from radio polarimetry data and the central density calculated from the *Chandra* observations, we can also estimate the magnetic field strength in the surrounding ICM. From the maximum absolute RM of  $125 \text{ rad m}^{-2} = 30 \times (1+z)^2$  and central density of  $0.016_{-0.001}^{+0.002} \text{ cm}^{-3}$  in the central 50 kpc, we derive a minimum magnetic field strength of  $0.2 \mu\text{G}$ . This is two orders of magnitudes

lower than has been found for some clusters (see review by Carilli & Taylor 2002) for which estimated magnetic fields in the range of  $10 - 40 \mu\text{G}$  are based on higher RMs (however see Rudnick & Blundell 2003 and Farnsworth et al. 2011). It is possible that this cluster is unusual or that there is evolution in the magnetic field strengths over time. However, we are confident of the veracity of the Rotation Measure inferred for PKS 1229-021, since this is done from closely-spaced frequencies having well-matched resolution.

## 6 IMPLICATIONS FOR CLUSTER SURVEYS

As discussed in the Introduction, strong cool-core clusters appear to be uncommon at  $z > 0.5$  (Vikhlinin et al. 2007; Santos et al. 2008). We investigate here whether surveys searching for strong cool cores at high redshift could be affected by a selection effect, in which strong cool cores are lost due to the presence of a quasar in the brightest cluster galaxy (BCG).

All low redshift cool core clusters are relatively relaxed and centred on a BCG with an active nucleus. Most of these nuclei are best seen at radio wavelengths due to the jets which power the heating of the cool core and balance the radiative cooling taking place (for reviews see Peterson & Fabian 2006; McNamara & Nulsen 2007). Some are powerful (e.g. Cygnus A) and just one is a quasar (H1821+643; Russell et al. 2010). Quasars are more common at higher redshift, so it is plausible to assume that they are more common in BCG hosts too. If this occurs, then the quasar can dominate the X-ray emission, leading to the object being classified only as a quasar in a survey image from, e.g. ROSAT. There is already evidence for clusters at the level of  $\sim 10^{44} \text{ erg s}^{-1}$  underlying several radio galaxies and radio-loud quasars at  $0.5 < z < 1$  (Crawford & Fabian 1996, 2003; Worrall et al. 2003; Belsole et al. 2007). 3C 186 is an excellent example of a cool-core cluster surrounding a radio-loud quasar at  $z \sim 1$  (Siemiginowska et al. 2005, 2010).

Whether a significant number of high redshift cool core cluster can be missing from X-ray surveys, due to the emission being swamped by a central quasar, depends on the surface densities of the objects and how the survey is conducted. Wolter & Celotti (2001) report on the surface density of radio-loud quasars, yielding about one per 6 sq deg with X-ray luminosity  $L_x > 10^{44} \text{ erg s}^{-1}$ , and  $0.5 < z < 1.5$ , and about 10–20 times fewer at  $L_x > 10^{45} \text{ erg s}^{-1}$ , say about one per 60 sq deg or so. Rapetti et al. (2008) estimate that the number of clusters with  $L_x > 3 \times 10^{44} \text{ erg s}^{-1}$ , and  $0.5 < z < 1.5$ , is about one per 20 sq deg. Strong cool core clusters are about one third of all clusters at low redshift, so for the maximal case of no evolution in that fraction, we expect about one strong cool core cluster per 60 sq deg. Although the number densities of these objects are only roughly comparable, we also note that a) the lower redshift quasar at the centre of a cluster, H1821+643, is (just) radio quiet (Blundell & Rawlings 2001), so we could include radio-quiet quasars as well which increases the numbers of quasars to be considered by up to a factor of ten; and b) the quasar luminosity required to cause a surrounding cluster to be lost in a survey will depend on the source selection but may not need to much exceed the core luminosity of the cluster. For relatively low spatial resolution surveys, the optical classification of an object can also be important as an object could be classified only as a quasar if broad lines are detected. We therefore suggest that selection effects could distort the observed fraction of strong cool core clusters identified in high redshift surveys but this will be dependent on the available angular resolution and how the survey is conducted.



## 7 CONCLUSIONS

Radio observations of the powerful  $z = 1.04$  quasar PKS 1229-021 show a strong core and a bright, one-sided jet leading to the SW hot spot and a second hot spot visible on the counter-jet side. Our 100 ks *Chandra* observation of this source also clearly reveals the presence of extended X-ray emission around the quasar. Although the wings of the quasar PSF provided a significant contribution to the total flux at all radii where the extended cluster emission was detected, we were able to accurately subtract off the PSF emission using ChaRT and MARX simulations. The extended cluster emission can be traced out to  $\sim 15$  arcsec ( $\sim 120$  kpc) radius and appears to have a very steeply declining surface brightness profile. We compared the surface brightness profile for PKS 1229-021 with the profile from the FR II radio galaxy 3C 444, which has a similarly steep surface brightness drop caused by a powerful shock surrounding the radio lobes (Croston et al. 2010). Using a model surface brightness profile based on 3C 444, we estimated the total cluster luminosity for PKS 1229-021 to be  $L_X \sim 2 \times 10^{44}$  erg s $^{-1}$ . We calculated a hardness ratio profile for the extended emission in PKS 1229-021 and found a decline in the hardness ratio in the central 5 arcsec radius consistent with the presence of a cool core. X-ray emission associated with a bright quasar, such as PKS 1229-021, makes it very difficult to detect underlying cool core clusters at high redshift. We suggest that modest angular resolution surveys of strong cool core clusters at high redshift could be affected by this selection effect.

## ACKNOWLEDGEMENTS

HRR acknowledges generous financial support from the Canadian Space Agency Space Science Enhancement Program. ACF thanks the Royal Society for support. GBT acknowledges support for this provided by the National Aeronautics and Space Administration through Chandra Award Number GO0-11139X issued by the Chandra X-ray Observatory Center, which is operated by the Smithsonian Astrophysical Observatory for and on behalf of the National Aeronautics Space Administration under contract NAS8-03060. HRR thanks Brian McNamara for helpful discussions. We thank the referee for helpful and constructive comments. We also thank Mark Bautz for suggesting the use of the ACIS readout streak to extract the source count rate and the *Chandra* X-ray Center for the analysis and extensive documentation available on the *Chandra* PSF.

## REFERENCES

Allen S. W., et al., 2001, MNRAS, 324, 842  
 Alshino A., Ponman T., Pacaud F., Pierre M., 2010, MNRAS, 407, 2543  
 Anders E., Grevesse N., 1989, Geochim. Cosmochim. Acta, 53, 197  
 Arnaud K. A., 1996, in Astronomical Society of the Pacific Conference Series, Vol. 101, Jacoby G. H., Barnes J., ed, Astronomical Data Analysis Software and Systems V, p. 17  
 Arnaud K. A., Fabian A. C., Eales S. A., Jones C., Forman W., 1984, MNRAS, 211, 981  
 Balucinska-Church M., McCammon D., 1992, ApJ, 400, 699  
 Bauer F., Fabian AC., Johnstone RM., Allen, SW., 2005, MNRAS 368, 1735  
 Belsole E., Worrall D. M., Hardcastle M. R., Croston J., 2007, MNRAS, 381, 1109  
 Böhringer H., Burwitz V., Zhang Y., Schuecker P., Nowak N., 2005, ApJ, 633, 148  
 Blundell K. M., Rawlings S., 2001, ApJ, 562, L5

Carilli C. L., Taylor G. B., 2002, ARA&A, 40, 319  
 Carter C., Karovska M., Jerius D., Glotfelty K., Beikman S., 2003, in Astronomical Society of the Pacific Conference Series, Vol. 295, Payne H. E., Jedrzejewski R. I., Hook R. N., ed, Astronomical Data Analysis Software and Systems XII, p. 477  
 Cash W., 1979, ApJ, 228, 939  
 Cavaliere A. & Fusco-Femiano R., 1976, A&A, 49, 137  
 Celotti A., Fabian A. C., 2004, MNRAS, 353, 523  
 Celotti A., Ghisellini G., 2008, MNRAS, 385, 283  
 Crawford C. S., Fabian A. C., 2003, MNRAS, 339, 1163  
 Crawford C. S., Fabian A. C., 1996, MNRAS, 282, 1483  
 Croston J. H., Hardcastle M. J., Mingo B., Evans D. A., Dicken D., Morganti R., Tadhunter C. N., 2011, ApJ, 734, 28  
 Croston J. H., Hardcastle M. J., Harris D. E., Belsole E., Birkinshaw M., Worrall D. M., 2005, ApJ, 626, 733  
 Croton D., et al., 2006, MNRAS, 367, 864  
 Davis J. E., 2001, ApJ, 562, 575  
 Erlund M. C., Fabian A. C., Blundell K. M., 2008, MNRAS, 386, 1774  
 Fabian A.C., Celotti, A., Blundell K.M., Kassim NE., Perley RA., 2002, MNRAS, 331, 369  
 Fabian A.C., Sanders J.S., Crawford C.S., Ettori S., 2003, MNRAS, 341, 729  
 Fanaroff B. L., Riley J. M., 1974, MNRAS, 167, 31P  
 Farnsworth D., Rudnick L., Brown S., 2011, AJ, 141, 191  
 Fomalont E. B., et al., 2000, ApJS, 131, 95  
 Freeman P. E., Kashyap V., Rosner R., Lamb D. Q., 2002, ApJS, 138, 185  
 Fruscione A. et al., 2006, in Presented at the Society of Photo-Optical Instrumentation Engineers (SPIE) Conference, Vol. 6270, Society of Photo-Optical Instrumentation Engineers (SPIE) Conference Series  
 Gaetz T. J., 2010, Analysis of the *Chandra* On-Orbit PSF Wings, <http://cxc.harvard.edu/cal/Hrma/PSFWings.html>  
 Hall P. B., Green R. F., 1998, ApJ, 507, 558  
 Henry J. P., Henriksen M. J., 1986, ApJ, 30, 689  
 Jerius D., 2002, Comparison of on-axis *Chandra* Observations of AR Lac to SAOSac Simulations, <http://cxc.harvard.edu/cal/Hrma/rsrc/Public/PSFCore/ARLac-onaxis.pdf>  
 Jerius D., Freeman M., Gaetz T., Hughes J. P., Podgorski W., 1995, in Astronomical Society of the Pacific Conference Series, Vol. 77, Shaw R. A., Payne H. E., Hayes J. J. E., ed, Astronomical Data Analysis Software and Systems IV, p. 357  
 Kaastra J. S., 1992, in Internal SRON-Leiden Report, updated version 2.0  
 Kalberla P. M. W., Burton W. B., Hartmann D., Arnal E. M., Bajaja E., Morras R., Pöppel W. G. L., 2005, A&A, 440, 775  
 Kovalev Y. Y., Petrov L., Fomalont E. B., Gordon D., 2007, AJ, 133 1236  
 Kronberg P. P., Perry J. J., Zukowski E. L. H., 1992, ApJ, 387, 528  
 Landau L. D., Lifshitz E. M., 1959, Fluid mechanics, Oxford, Pergamon Press  
 Liedahl D. A., Osterheld A. L., Goldstein W. H., 1995, ApJ, 438, L115  
 Lumb D. H., et al., 2004, A&A, 420, 853  
 Markevitch M., Vikhlinin A., 2007, Phys. Rep., 443, 1  
 Marshall H. L., et al., 2005, ApJS, 156, 13  
 McNamara B. R., Nulsen P. E. J., 2007 ARAA, 45, 117  
 Mewe R., Gronenschild E. H. B. M., van den Oord G. H. J., 1985, A&AS, 62, 197  
 Mewe R., Lemen J. R., van den Oord G. H. J., 1986, A&AS, 65, 511  
 O'Dea C., et al., 2008, ApJ, 681, 1035  
 Park T., Kashyap V. L., Siemiginowska A., van Dyk D. A., Zezas A., Heinke C., Wargelin B. J., 2006, ApJ, 652, 610  
 Peres C., et al., 1998, MNRAS, 298 416  
 Peterson J., Fabian A. C., 2006, Phys Rep, 427, 1  
 Pratt G. W., Croston J. H., Arnaud M., Böhringer H., 2009, A&A, 498, 361  
 Rafferty D. A., McNamara B. R., Nulsen P. E. J., 2008, ApJ, 687, 899  
 Rapetti D., Allen S. W., Mantz A., 2008, MNRAS, 388, 1265  
 Reynolds C. S., Fabian A. C., 1996, MNRAS, 278, 479  
 Rudnick L., Blundell K. M., 2003, ApJ, 588, 143  
 Russell H. R., Fabian A. C., Sanders J. S., Johnstone R. M., Blundell K. M., Brandt W. N., Crawford C. S., 2010, MNRAS, 402, 1561

- Samuele R., McNamara B. R., Vikhlinin A., Mullis C. R., 2011, *ApJ*, 731, 31
- Sanders, JS, Fabian AC, 2006, *MNRAS*, 371, L65
- Santos, J. S., Rosati P., Tozzi P., Böhringer H., Ettori S., Bignamini A., 2008, *A&A*, 483, 35
- Siemiginowska A., Burke D. J., Aldcroft T. L., Worrall D. M., Allen S., Bechtold J., Clarke T., Cheung C. C., 2010, *ApJ*, 722, 102
- Siemiginowska A., et al., 2005, *ApJ*, 632, 110
- Siemiginowska A., Smith R.K., Aldcroft T., Schwartz D.A., Paerels F., Petric A.O., 2003, *ApJ*, 598, L15
- Tavecchio F., Maraschi L., Wolter A., Cheung C. C., Sambruna R. M., Urry C. M., 2007, *ApJ*, 662, 900
- Taylor G. B., Fabian A. C., Allen S. W., 2002, *MNRAS*, 334, 769
- Thompson D. J., et al., 1995, *ApJS*, 101, 259
- Vikhlinin A., et al., 2007, Heating versus Cooling in Galaxies and Clusters of Galaxies, 48, astro-ph/0611438
- Vikhlinin A., et al., 2002, *ApJ*, 578, L107
- Wilkes B. J., et al., 2011, accepted by *ApJ*, astro-ph/1109.4395
- Wolter A., Celotti A., 2001, *A&A*, 371, 527
- Worrall D. M., Birkinshaw M., Hardcastle M. J., 2003, *MNRAS*, 343, 73
- Worrall D., Birkinshaw M., Hardcastle MR, Lawrence CR, 2001, *MNRAS*, 326, 1127